Published in Journal of Applied Physics," DOI: 10.1063/5.0264069, online on 15 July 2025
Vol. 138, No. 3

Oxygen impurity effects on the piezoelectric response of wurtzite $Al_{0.625}Sc_{0.375}N$

Xian Wang[1, †], Shashidhara Acharya[2, †], Peng Wang[3], Yi-Ming Zhao[4], Kui Yao[2] and Lei Shen[4, *]
[1]Chemical Engineering and Biotechnology, Nanyang Technological University, Singapore 637371, Singapore
[2]Institute of Materials Research and Engineering (IMRE), Agency for Science, Technology and Research (A*STAR), Singapore138634, Singapore
[3]College of Electronic and Information Engineering, Shandong University of Science and Technology, Qingdao 266590, China
[4]Department of Mechanical Engineering National University of Singapore, Singapore117575, Singapore
[*]Corresponding author: shenlei@nus.edu.sg

ABSTRACT

$Al_{1-x}Sc_xN$ thin films have attracted remarkable attention in industrial applications, including micro-electro-mechanical systems and radio frequency acoustic filters, due to their excellent piezoelectric properties and processing compatibility. However, a major challenge in developing high-performance $Al_{1-x}Sc_xN$ thin films lies in controlling persistent oxygen impurities. Here, we systematically investigate the impact of oxygen impurities on the structural stability and piezoelectric properties of experimentally reported wurtzite $Al_{0.625}Sc_{0.375}N$ using first-principles calculations. 17 types of defect configurations incorporating oxygen defects and cation vacancies have been developed, providing critical insights into their formation energies, effective piezoelectric coefficient ($d_{33,f}$), dielectric constant (ε_{33}) and electromechanical coupling coefficient (K_{33}^2). Our findings demonstrate that moderate oxygen doping, particularly oxygen substitutional defects (O_N), enhances the coefficient $d_{33,f}$ primarily attributed to a reduction in the elastic constant C_{33} and increase in the piezoelectric tensor e_{33}. In contrast, the interstitial oxygen (O_i) and cation vacancies ($V_{Al/Sc}$) tend to decrease $d_{33,f}$. Moreover, a low concentration pure O_N at about 1.6% can notably enhance $d_{33,f}$ and K_{33}^2 compared to oxygen-free w-$Al_{0.625}Sc_{0.375}N$ and a higher concentration of O_N defects increases ε_{33}, further boosting electric field response along c-axis. These insights into defect engineering in Sc-doped AlN provide promising strategies for enhancing piezoelectric performance.

I. INTRODUCTION

Aluminum nitride (AlN)-based materials are highly valued as piezoelectric thin films due to its balanced properties for high-frequency and low-noise applications, stable piezoelectricity at elevated temperatures, well-established sputtering deposition process[1-3]. However, the piezoelectric constant d_{33} of pure AlN is two orders in magnitude lower than that of lead zirconate titanate (PZT), which is commonly used in industrial applications[4]. Doping with transition metals is a well-established strategy for enhancing the piezoelectric properties of AlN[5-7]. Specifically, scandium (Sc) doping increases the piezoelectric response of intrinsic AlN by nearly 500%, positioning $Al_{1-x}Sc_xN$ as a promising material for advanced piezoelectric and ferroelectric device applications[8-12]. The Sc concentration is critical to determining the crystal phase of $Al_{1-x}Sc_xN$, and hence the piezoelectric coefficient[13-15]. First-principles calculations have shown that $Al_{1-x}Sc_xN$ prefers the wurtzite structure (*w*-$Al_{1-x}Sc_xN$), a hexagonal lattice with space group $P6_3mc$, at scandium concentrations below approximately 50%, while at higher Sc contents it tends to transition to the rock-salt structure (*r*-$Al_{1-x}Sc_xN$), a cubic (NaCl-type) phase[13]. Experimentally, it has been reported that wurtzite and rock-salt phases appear at different Sc concentrations, with the rock-salt phase fraction increasing as Sc concentration rises, and a sharp decline in piezoelectricity is observed around 50% Sc concentrations[8].

In addition to Sc concentration affecting piezoelectricity of $Al_{1-x}Sc_xN$, another crucial factor is impurities, particularly oxygen from source contamination or residual background gases (O_2, H_2O, CO_2) during thin-film deposition[16-17]. Meanwhile, Sc doping in AlN increases oxygen incorporation due to its high thermodynamic affinity for oxygen, especially at elevated Sc concentrations[18-20]. Oxygen impurities typically degrade the performance of AlN-based films by compromising structural integrity, promoting domain inversion boundaries, and generating charged point defects that alter dielectric and thermoelectric properties[21-23]. Consequently, both fundamental and applied research on the impact of oxygen impurities on the piezoelectric properties of $Al_{1-x}Sc_xN$ has attracted considerable interest.

It is worth noting that the introduction of oxygen into AlN-based materials form complex defects, such as oxygen substitutional defects, oxygen interstitial defects and cation vacancies, which further impact material performance together with the Sc doping[24-26]. Theoretically, Yan et al. [26] investigated the formation energy, transition levels, and optical properties of defects in *w*-AlN, with a focus on the cases of Al vacancies (V_{Al}), N vacancies (V_N), O doped N (O_N) and the complex defect of O_N-V_{Al}. Kumar et al.[25] investigated the formation of oxygen defects in *r*-$Al_{1-x}Sc_xN$, focusing on O_N, interstitial oxygen (O_i), and combined substitutional and interstitial oxygen (O_N+O_i) configurations, showing that *r*-$Al_{1-x}Sc_xN$ prefers to be in the defect complex of $nO_N + O_i$ types. Experimentally, positron annihilation studies have revealed that in as-grown *w*-AlN samples, the O_N-V_{Al} is the predominant form of V_{Al}, whereas isolated V_{Al} defects are primarily detected in irradiated samples[27]. Electron paramagnetic resonance measurements have identified defects on the N sublattice, specifically O_N or V_N sites, providing additional insight into defect structures within *w*-AlN[28-29]. Notably, earlier studies have primarily focused the defects in pure AlN.

Recent computational investigations have demonstrated that oxygen impurities can profoundly affect ferroelectric behavior of $Al_{1-x}Sc_xN$-based systems[30,31]. These insights highlight the critical role of defect engineering in tuning the functional properties of $Al_{1-x}Sc_xN$. Beyond ferroelectricity, the piezoelectric response of $Al_{1-x}Sc_xN$ is particularly susceptible to

defect-induced variations, as both the polarization magnitude and lattice distortions contribute significantly to its electromechanical performance. Consequently, elucidating the influence of oxygen-related defects on the piezoelectric properties of $Al_{1-x}Sc_xN$ is essential for guiding the optimization of its practical applications. However, comprehensive investigations into the impact of defects, particular oxygen impurities, on the structural and piezoelectric properties of Sc-doped *w*-AlN films are still limited. In this work, we systematically investigate the effects of oxygen-related defects on the structural stability, piezoelectric response, and dielectric properties of experimentally reported *w*-$Al_{1-x}Sc_xN$ using density functional theory (DFT). While our previous study[32] primarily correlated experimental measurements with first-principles analysis for selected defect scenarios in *w*-$Al_{0.65}Sc_{0.35}N$ thin films, the present work overcomes prior limitations by systematically constructing and evaluating 17 representative defect types—including substitutional and interstitial oxygen, their complexes, and vacancy-assisted forms. We assess their influence on key physical quantities such as elastic constants, piezoelectric tensors, dielectric permittivity, and electromechanical coupling coefficients. Furthermore, by decomposing the piezoelectric tensor into electronic and ionic components, we uncover the microscopic mechanisms through which specific oxygen-related defects modulate functional responses. This comprehensive theoretical framework provides critical insights into the defect–property relationship in Sc-doped AlN and offers practical guidance for defect engineering in wurtzite nitride-based piezoelectric devices.

II. METHODS

All the first-principles calculations were performed using DFT method within the Vienna Ab-initio Simulation Package (VASP)[33,34]. Electron-core interactions were modeled with the projector-augmented wave (PAW) method, utilizing a plane wave basis set[35]. The exchange-correlation effects were treated using the generalized gradient approximation (GGA) with the Perdew–Burke–Ernzerhof (PBE) functional[36,37], and dispersion corrections were incorporated through Grimme's DFT-D3 method to account for weak interatomic interactions, particularly those introduced by oxygen-related defects[38]. An energy cutoff of 600 eV was used, with full structural optimization conducted until atomic forces converged below 0.01 eV/Å. The electronic convergence criterion was set to 10^{-6} eV, and a Monkhorst-Pack k-point mesh of 4×4×4 was used for Brillouin zone sampling[39].

The formation energy (E_F) is calculated using the Zhang–Northrup scheme[40], as defined by:

$$E_f(def) = E(A_{defect}) - E(A_{perfect}) + \sum_i n_i \mu_i \quad (1)$$

Here, $E(A_{defect})$ denotes the total energy of the supercell containing defects, while $E(A_{perfect})$ is the total energy of the pristine supercell. The variables μ_i represent the chemical potential of each element added to or removed from the pristine supercell to create the defect supercell, and n_i indicates the number of atoms added (or removed) to form the defect. The chemical potentials are carefully selected to ensure the thermodynamic stability of defective *w*-$Al_{1-x}Sc_xN$ with respect to competing phases under representative O-rich and O-poor conditions, although they are not derived from a complete thermodynamic phase diagram —a more rigorous framework for predicting phase stability[30]. For nitrogen-rich conditions, the chemical potential of nitrogen μ_N is determined using Eq. (2), given by:

$$\mu_N = E_{tot}(N) - D_0(N) \quad (2)$$

The chemical potential of oxygen is calculated under both oxygen-rich and oxygen-poor conditions, as defined in Eqs. (3) and (4). Under oxygen-rich conditions,

$$\mu_O = E_{tot}(O) - D_0(O) \quad (3)$$

Under oxygen-poor conditions, the chemical potential of oxygen μ_O, is determined by the following equation:

$$\mu_O = \frac{1}{3}(E_{tot}(Sc_2O_3/Al_2O_3)) - 2 \times \mu_{Sc/Al} \quad (4)$$

$E_{tot}(N)$ and $E_{tot}(O)$ represent the atomic energies of nitrogen and oxygen, respectively, obtained by calculating a single atom with appropriate spin polarization in a cubic supercell with at least 25 Å of vacuum along each axis[25]. The values $D_0(N)$ and $D_0(O)$ are the experimental dissociation energies of nitrogen (9.80 eV) and oxygen (5.16 eV), respectively, as reported by Huber and Herzberg[41]. Determining the appropriate reference under oxygen-poor conditions is challenging, as it could be either Sc_2O_3 or Al_2O. Therefore, we considered both conditions. E_{tot} (Sc_2O_3/Al_2O_3) refers to the total energy of Sc_2O_3 or Al_2O_3 in the cubic or hexagonal crystal structure, while μ_{Sc} and μ_{Al} represent the chemical potentials of scandium and aluminum in their metallic forms. This approach provides a more accurate calculation of the chemical potentials of O and N compared to the conventional method, which derives μ_N and μ_o from the total energy of O_2 or N_2 molecules in a supercell. The chemical potentials of O and N were determined under O-rich and N-rich limits, respectively, consistent with typical experimental growth conditions and prior investigations of oxygen-related defects in r-$Al_{1-x}Sc_xN$ [25,32]. Here, defect formation energies were computed based on static DFT total energies without explicitly incorporating entropy contributions. While this approach provides valuable qualitative insights into defect behavior, its omission of entropy contributions inherently limits the quantitative accuracy of thermodynamic stability predictions at finite temperatures, where entropic effects can play a critical role in stabilizing certain alloy phases and defect complexes under realistic synthesis conditions[30,42]. Therefore, the results presented here should be interpreted as representative of low-temperature or entropy-neglected scenarios, and care should be taken when extrapolating to high-temperature growth environments.

Moreover, the piezoelectric tensors e_{ij} and the Born effective charges (Z_{ij}^*) are predicted by Density Functional Perturbation Theory (DFPT) method[43]. Convergence tests were performed on w-AlN using a high-precision electronic convergence of 10^{-7} eV and Monkhorst–Pack k-point meshes of 4×4×4 and 8×8×8. As shown in Tables. SI-VI, the calculated piezoelectric tensors values were very close, confirming good convergence. Based on this, a 4×4×4 k-point mesh was adopted to ensure reliable convergence while balancing computational cost. The elastic constant C_{33} for $Al_{1-x}Sc_xN$ is determined by applying strain along the c-axis and fitting the resulting energy-strain curve. This is done by modifying the lattice parameters with strains (-0.015, -0.010, -0.005, 0.00, +0.015, +0.010, +0.005) and extracting C_{33} from the slope of curve via the second derivative of a polynomial fit to the calculated energies. The effective piezoelectric coefficient $d_{33,f}$ could be defined as:

$$d_{33,f} = \frac{e_{33}}{C_{33}} \quad (5)$$

III. RESULTS

Based on experimentally reported w-$Al_{0.625}Sc_{0.375}N$ thin films[32], we investigate the effects of oxygen defects (ranging from 1% to 4.8%) and cation vacancies under various conditions on

the structural and piezoelectric properties of the material, focusing on 17 favorable defects, O_N-O_i and $V_{Al/Sc}$-$O_{N/i}$. For O_N-O_i type, there are 7 cases: $1O_N$, $1O_i$, $2O_N$, $1O_N$+$1O_i$, $3O_N$, $2O_N$+$1O_i$, $1O_N$+$2O_i$, where O_N means replacing N atoms by O atoms, O_i is the interstitial O atoms. For complex $V_{Al/Sc}$-$O_{N/i}$, there are 10 cases: $1O_N$+$V_{Al/Sc}$, $2O_N$+$V_{Al/Sc}$, $1O_N$+$1O_i$+$V_{Al/Sc}$, $3O_N$+$V_{Al/Sc}$, $2O_N$+$1O_i$ +$V_{Al/Sc}$), where $V_{Al/Sc}$ means Al or Sc vacancies. The candidate structures were constructed using the equivalent-site substitution method. For every best composition, which has the lowest energy, was screened using a multistep approach using DFT method and sent to subsequent property calculations, as detailed in Fig. S1. The calculated lattice parameters and internal parameter u are presented in Table SVII, where u represents the ratio of the lattice constant c to the cation–anion (Al/Sc–N/O) bond length along the c-axis. These lattice parameters closely match those observed in experiments[32]. Notably, the internal parameter for Sc-N/O bonding is larger than that of Al-N/O bonding. Additionally, the defect formation energy (E_F) as a function of difference oxygen chemical potential ($\Delta\mu_O$) for various oxygen defect configurations in w-$Al_{0.625}Sc_{0.375}N$ is calculated, as shown in Tables SVIII-SXI. Here, $\Delta\mu_O$ represents the chemical potential difference referenced to the chemical formula under O-rich conditions. In oxygen-poor conditions, μ_O is calculated using Al_2O_3 and Sc_2O_3 as reference materials, aligning with approaches used in previous studies[25-26]. As depicted in Fig. 1 and Fig. S2, the trend observed using Al_2O_3 as a reference is similar to that obtained with Sc_2O_3. Here, Al_2O_3 is used as an example for further analysis. Defect formation energies were calculated to assess the relative stability of oxygen-related defects. The chemical potentials were constrained according to the Zhang–Northrup formalism[40] to ensure the thermodynamic stability of w-$Al_{0.625}Sc_{0.375}N$ against competing phases. Thus, the negative formation energies indicate a realistic tendency for oxygen incorporation during growth conditions, rather than spontaneous decomposition. Figure 1(a) presents the defect configurations involving O_N and O_i in w-$Al_{0.625}Sc_{0.375}N$. Under oxygen-poor conditions, all defect formation energies are positive, with minimum and maximum values of 2.04 eV and 12.43 eV, respectively, indicating these defects are energetically unfavorable and unlikely to form in such an environment. In contrast, under oxygen-rich conditions, all defects exhibit negative formation energies except for the $1O_i$ configuration, which remains positive with 1.30 eV. The negative formation energy reflects a thermodynamic tendency for the formation of oxygen-related defects under oxygen-rich conditions. The lowest formation energy is observed for $2O_N$+$1O_i$ at -5.33 eV, followed by $3O_N$ at -4.33 eV, $2O_N$ at -2.81 eV, $1O_N$ at -1.38 eV, and $1O_N$+$2O_i$ at -0.240 eV. These values suggest that, in oxygen-rich conditions, the $2O_N$+$1O_i$ configuration is the most favorable, with other four configurations also potentially forming. Moreover, the combination of O_N and O_i defects is favorable for reducing the formation energy in oxygen-rich environments. A single O_i defect tends to have larger formation energy and is thus relatively unfavorable. However, the formation energy decreases when $1O_N$ and $1O_i$ coexist, and it further decreases as the number of O_N atoms increases. This trend is consistent with findings from similar theoretical studied for rock-salt phase[25].

For defect configurations that involve oxygen defects in combination with Al or Sc vacancies, as shown in Fig. 1(b), all configurations except $3O_N$+$V_{Al/Sc}$ exhibit positive formation energies in both oxygen-poor and rich conditions. This indicates that these configurations are energetically unfavorable and unlikely to form in either condition. In the case of $3O_N$+$V_{Al/Sc}$, the formation energies are positive under oxygen-poor conditions, at 4.63

eV and 5.50 eV, but become negative under oxygen-rich conditions, at -5.62 eV and -4.74 eV. This suggests that, among oxygen defects and cation vacancies, the $3O_N+V_{Al}$ configuration is the most favorable and thus potentially present in an oxygen-rich environment. Our results are consistent with findings from other studies[25]. Notably, the formation energies of $2O_N+1O_i$ and $3O_N+V_{Al}$ are relatively close, indicating that these two configurations are the most likely defect structures to form under oxygen-rich conditions. These trends provide valuable insights into the stability of oxygen defects in *w*-$Al_{0.625}Sc_{0.375}N$ under varying oxygen environments, which is critical for tailoring the properties of *w*-$Al_{1-x}Sc_xN$ for specific applications.

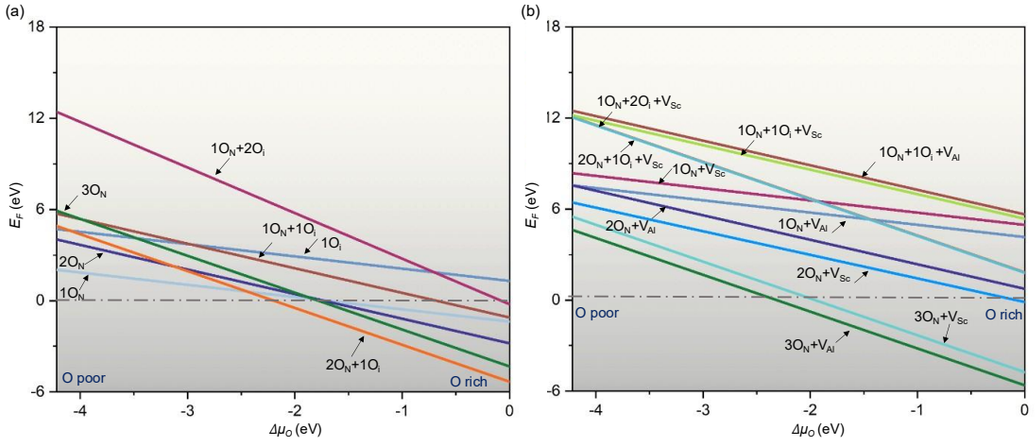

FIG. 1. (a) Defect formation energy (E_F) as a function of difference oxygen chemical potential ($\Delta\mu_O$) for various O defect configurations with (a) O_N-O_i and (b) $O_{N/i}$-$V_{Al/Sc}$ in *w*-$Al_{0.625}Sc_{0.375}N$ taking Al_2O_3 as a reference for O poor condition. $\Delta\mu_O$ represents the chemical potential difference referenced to the chemical formula under O-rich conditions.

Based on the formation energy analysis above, various O_N-O_i and $3O_N+V_{Al/Sc}$ configurations are selected to calculate piezoelectric properties and assess their impact on the piezoelectric performance of *w*-$Al_{0.625}Sc_{0.375}N$. The detailed piezoelectric calculations are included in the SM. Figure 2(a) illustrates the relationship between the effective piezoelectric coefficient $d_{33,f}$ and oxygen concentration across different defect configurations. The calculated effective piezoelectric coefficient $d_{33,f}$ for pure *w*-$Al_{0.625}Sc_{0.375}N$ is 16.21 pm/V, which closely matches previous theoretical results (approximately 14 pm/V) reported at similar Sc concentrations using the effective coefficient approach, while being lower than those obtained via the complete tensor method[44,45]. To capture the experimentally relevant oxygen concentrations, we selected favorable defect configurations, $1O_N$ (1.6%), $2O_N$ (3.1%) and $3O_N+V_{Al}$ (4.8%), which exhibit a consistent decrease in piezoelectric response with increasing oxygen concentration, in agreement with experimental trends[32]. Our study reveals that moderate oxygen concentrations ($1O_N$, at 1.6%) can actually enhance the piezoelectric coefficient, with an increase of approximately 1.5 times relative to the oxygen-free state[32]. For various oxygen defects, O_N defects contribute to enhanced piezoelectric properties. Conversely, at comparable oxygen concentrations, O_i defects tend to reduce the piezoelectric coefficient. The presence of cation vacancies also leads to a decrease in the piezoelectric coefficient.

Furthermore, the response of $d_{33,f}$ to oxygen concentration is determined by the elastic constant C_{33} and the piezoelectric coefficient e_{33}, as shown in Figs. 2(b), 2(c) and Tables SXII-

SXLI, Table SXLV. The trend of e_{33} aligns with that of $d_{33,f}$, while the trend of C_{33} is opposite to that of $d_{33,f}$. This conclusion is also supported by other studies that the enhancement in $d_{33,f}$ is primarily attributed to the softening of the C_{33} and the increase in e_{33}[7, 44,46]. O_i and cation vacancies lead to a remarkable increase in C_{33} and a pronounced decrease in e_{33}, whereas O_N exhibit the opposite trend. This contrast underscores the critical influence of oxygen site occupancy and cation vacancies in shaping the piezoelectric performance of *w*-$Al_{0.625}Sc_{0.375}N$. These findings emphasize the importance of defect site characteristics in modulating piezoelectric properties.

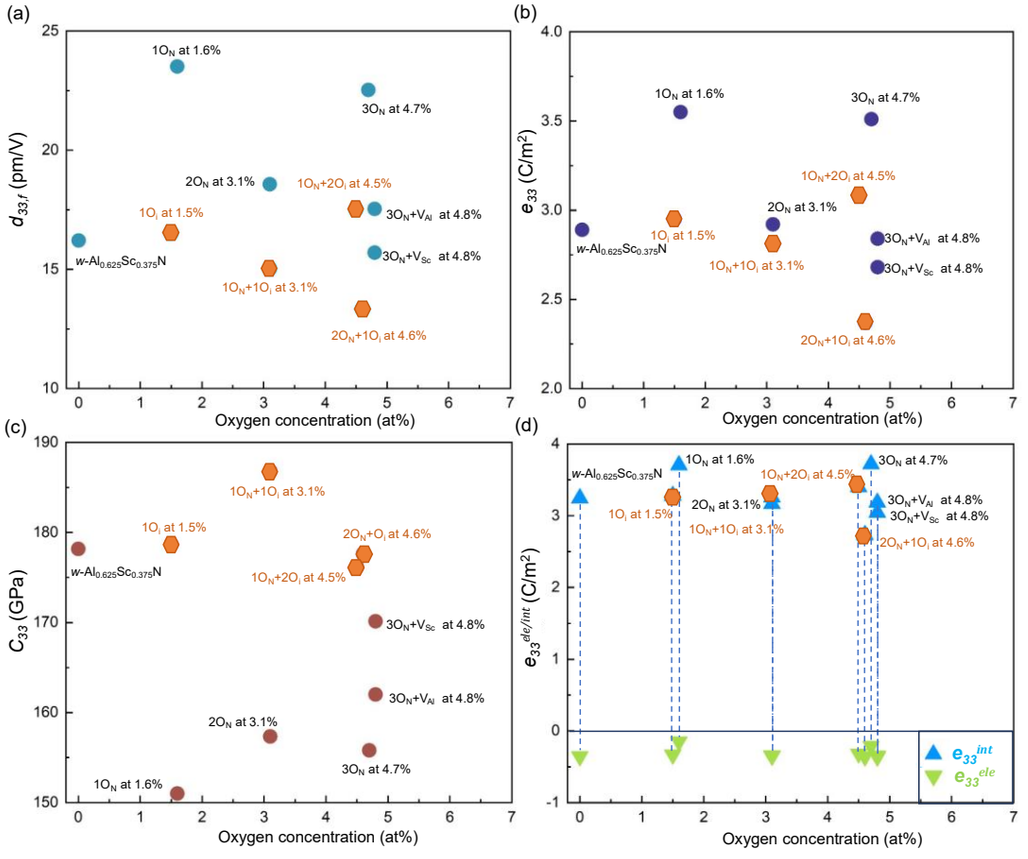

FIG. 2. (a) $d_{33,f}$(pm/V), (b) e_{33} (C/m^2), (c) C_{33} (GPa) and (d) e_{33}^{ele} and e_{33}^{int} (C/m^2) for different oxygen defects in $Al_{0.625}Sc_{0.375}N$. The orange hexagonal marker represents the O_i case type.

To elucidate the origin of the change in e_{33}, we express e_{33} ($e_{33} = e_{33}^{ele} + e_{33}^{int}$), where e_{33}^{ele} denotes the electronic contribution and e_{33}^{int} represents the contribution from the internal atomic coordinates in response to an external strain along the *c*-axis (η_3)[46-48]. This finding reveals that the variation in e_{33} is predominantly governed by e_{33}^{int}. For instance, the notable decrease in e_{33} results from a marked reduction in e_{33}^{int}, combined with an increase in the magnitude of e_{33}^{ele}, as the oxygen concentration increases from 1% to 4.8% (see Fig. 2(d)). Thus, the factors influencing e_{33}^{int} are further analyzed, as illustrated in Fig. 3. Structurally, as shown in Fig. 3(a), the average bond lengths of cations and anions vary with oxygen concentration and defect site, indicating notable changes in Sc–O and Al–O bond lengths. To gain deeper insights, the piezoelectric coefficient e_{33}^{int} is analyzed, as it is directly

proportional to two key factors: Born effective charge (Z_{33}) and the sensitivity of the atomic positions (μ_3) in response to the strain along *c*-direction ($\frac{d\mu_3}{d\eta_3}$). For the wurtzite structure, $e_{33}^{int} = \sum_i \frac{2e}{\sqrt{3}a^2} Z_{33}(i) \frac{\partial \mu_3}{\partial \eta_3}$, where *i* runs over all atoms in the supercell, *a* is the in-plane lattice parameter of the supercell, and *e* is the electron charge[47-49]. To simplify the analysis, it is practical to consider an average value of Z_{33} (Z_{33}^*) and $\frac{d\mu_3}{d\eta_3}$ ($\frac{d\mu_3}{d\eta_3}^*$) rather than individual atomic contributions within a large supercell. In Fig. 3(b) and Table SXLII, we present the Z_{33}^* for each atom type (k) in the supercell, defined as $Z_{33}^*(k) = \frac{1}{n_k}\sum_{n_k} Z_{33}(n_k)$, n_k runs over all atoms of type k within supercell (e.g., n_{Al}, n_{Sc}, n_N, n_O). Similarly, we take the $\frac{d\mu_3}{d\eta_3}^*$ as shown in Fig. 3(c), and Table SXLIII, defined as $\frac{d\mu_{3(k)}}{d\eta_3}^* = \frac{1}{n_k}\sum_{n_k} \frac{d\mu_3(n_k)}{d\eta_3}$. Analysis reveals that Z_{33}^* for O exhibits substantial variation with increasing oxygen concentration, followed by notable changes in Sc. In contrast, Z_{33}^* for Al and N remains largely stable, showing minimal response to changes in oxygen concentration. These findings indicate that the observed variations in Z_{33}^* are predominantly driven by contributions from O and Sc ions.

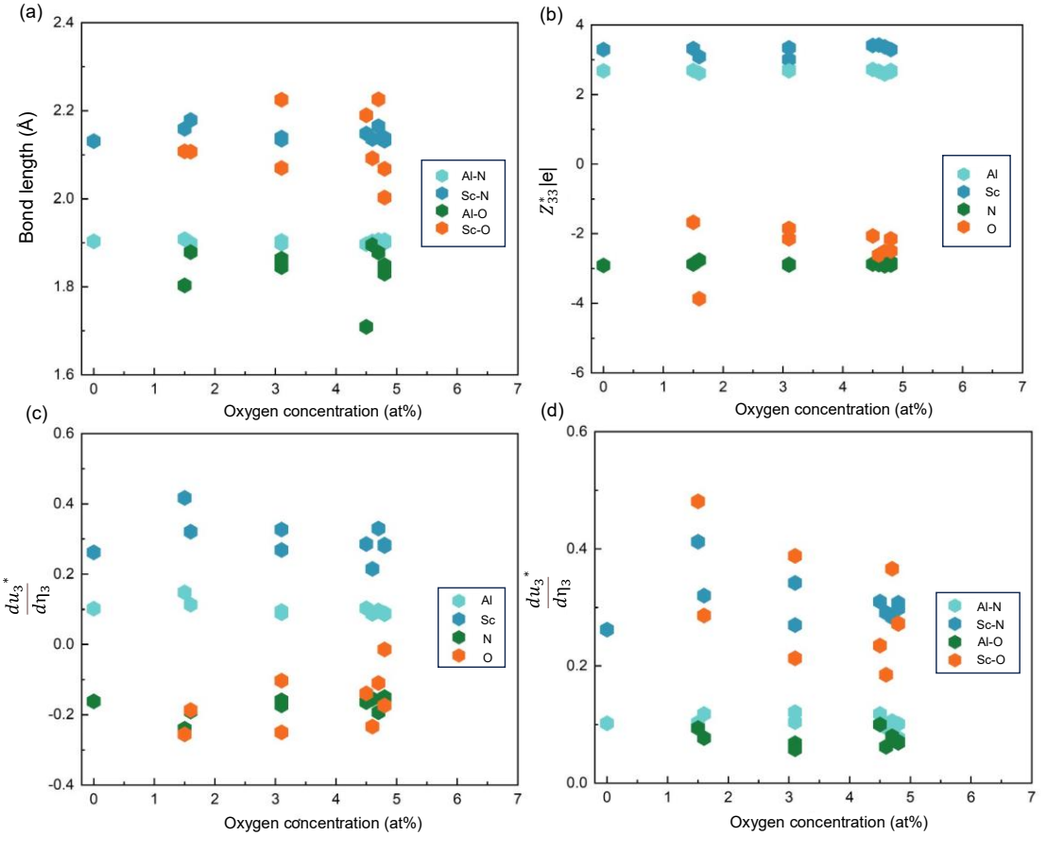

FIG. 3. (a) The average bond length, (b) average Born effective charge (Z_{33}*) and (c) average sensitivity of internal parameter ($\frac{d\mu_3}{d\eta_3}^*$) (d) $\frac{d\mu_3}{d\eta_3}^*$ of Al/Sc site bonded to O ($\frac{d\mu_3}{d\eta_3}^*$ (Al, O) and

$\frac{d\mu_3}{d\eta_3}^*$ (Sc, O) and bonded to N in the vicinity of defects at Al/Sc ($\frac{d\mu_3}{d\eta_3}^*$ (Al, N) and $\frac{d\mu_3}{d\eta_3}^*$ (Sc, N) as functions of oxygen concentrations in studied oxygen-related defects *w*-$Al_{0.625}Sc_{0.375}N$.

Furthermore, we monitored the $\frac{d\mu_3}{d\eta_3}^*$ of Al/Sc site bonded to O ($\frac{d\mu_3}{d\eta_3}^*$ (Al, O) and $\frac{d\mu_3}{d\eta_3}^*$ (Sc, O) and bonded to N in the vicinity of defects at Al/Sc ($\frac{d\mu_3}{d\eta_3}^*$ (Al, N) and $\frac{d\mu_3}{d\eta_3}^*$ (Sc, N) with oxygen concentration, as depicted in Fig. 3(d) and Table SXLIV. Our findings reveal that the most notable variations occur in Sc–O, followed by Sc–N, then Al–O, with Al–N showing minimal change, emphasizing the influence of Sc and O on the $d_{33,f}$ value. This relationship highlights the dependence of e_{33}^{int} on both the Born effective charge and atomic displacement sensitivity, which together contribute to the piezoelectric response in oxygen-defect configurations.

Sc-doping AlN-based piezoelectric materials are used in various applications, such as transducers, energy harvesting devices, pressure sensors[50,51]. For these applications, maintaining an appropriate band gap is crucial to ensure device performance and reliability. As shown in Table SXLVI, the calculated band gaps show that the introduction of oxygen-related defects and cation vacancies reduces the band gap of *w*-$Al_{0.625}Sc_{0.375}N$. However, as the defect concentration increases, the band gap decreases significantly, reaching as low as 0.87 eV for the configuration with three O_N defects. In contrast, the incorporation of Al or Sc vacancies together with oxygen defects partially restores the band gap (2.43–2.74 eV), suggesting that defect complex formation can mitigate the electronic degradation caused by excessive oxygen doping. Moreover, a high electromechanical coupling coefficient (K_{33}^2) is generally desired to achieve broader bandwidth, improved axial resolution, and enhanced sensitivity[52,53]. Figure 4(a) shows the coefficient K_{33}^2 of *w*-$Al_{0.625}Sc_{0.375}N$ under various oxygen defects and concentrations, which is defined as $K_{33}^2 = \frac{e_{33}^2}{\varepsilon_{33}C_{33}+e_{33}^2} \times 100\%$, where ε_{33} is a component of the dielectric tensor (illustrated in Table SXLV)[54]. The calculated K_{33}^2 value of about 28% for *w*-$Al_{0.625}Sc_{0.375}N$ in the absence of oxygen impurities, which is similar to previously reported 23% in the same composition[44]. Experimental measurements indicate electromechanical coupling coefficients of 10% and 15% for Sc doping concentrations of 20% and 30%, respectively, showing that increasing the Sc doping concentration tends to enhance K_{33}^2 of *w*-$Al_{1-x}Sc_xN$[55]. Compared with *w*-$Al_{0.625}Sc_{0.375}N$, this finding indicates that $1O_N$ at about 1.6% provides the most substantial enhancement of K_{33}^2, increasing it by 26%, followed by $3O_N$ and $3O_N+V_{Al}$, whereas $2O_N+1O_i$ notably reduces K_{33}^2, reducing it by 30%. This is attributed to the varying impacts of different oxygen defects on elastic, piezoelectric and dielectric constants. These results suggest that carefully optimizing oxygen defect configurations and concentrations is essential for maximizing K_{33}^2.

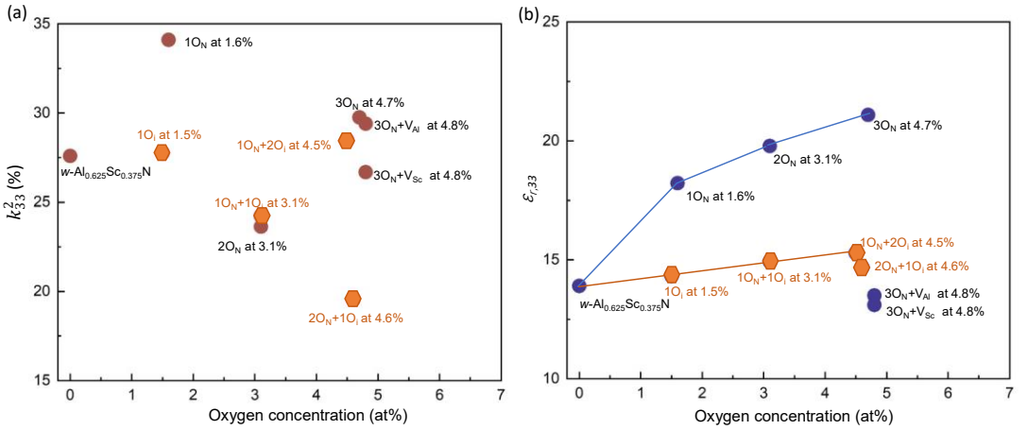

FIG. 4. (a) Longitudinal electromechanical coupling constant (K_{33}^2) and (b) the *c*-component of the relative macroscopic dielectric tensor ($\varepsilon_{r,33}$) as functions of oxygen concentrations in *w*-$Al_{0.625}Sc_{0.375}N$. The orange hexagonal marker represents the O_i case type.

Moreover, a larger dielectric tensor $\varepsilon_{r,33}$, indicates a stronger dielectric response of the material along the *c*-axis. Under an external electric field in *c*-axis, d_{33} represents the strain response of the material in the *c*-axis, while $\varepsilon_{r,33}$ describes the ability of material to polarize in response to the electric field in that direction. As $\varepsilon_{r,33}$ increases, the material becomes more easily polarized under an electric field. As shown in Fig. 4(b), O_N and O_i tend to enhance $\varepsilon_{r,33}$ in *w*-$Al_{0.625}Sc_{0.375}N$, whereas $V_{Al/Sc}$ generally reduces $\varepsilon_{r,33}$. The effect of O_N is notably stronger than that of O_i. As the number of O_N defects and the oxygen concentration increase, $\varepsilon_{r,33}$ also increases. Notably, $3O_N$ produces the most substantial enhancement of $\varepsilon_{r,33}$, increasing it by 55% compared to oxygen-free *w*-$Al_{0.625}Sc_{0.375}N$. Compared to the most stable $3O_N+V_{Al}$ configuration, $\varepsilon_{r,33}$ shows an increase of 56% for the $3O_N$ configuration. Our results indicate that increasing O_N concentration in *w*-$Al_{0.625}Sc_{0.375}N$ can enhance the dielectric constant in the *c*-axis, thereby increasing the sensitivity of material to electric stimuli.

IV. CONCLUSIONS

In conclusion, this study provides an in-depth analysis of the impact of oxygen-related defects on stability and the piezoelectric properties of experimental *w*-$Al_{0.625}Sc_{0.375}N$ using DFT calculations. The results reveal that under oxygen-rich conditions, the $3O_N+V_{Al}$ configuration is high stability and likelihood of formation. Our analysis of piezoelectric properties demonstrates that moderate oxygen doping, particularly oxygen substitutional defects, enhances the effective piezoelectric coefficient $d_{33,f}$, primarily by lowering the elastic constant C_{33} and increasing e_{33}. In contrast, the interstitial oxygen and cation vacancies tend to decrease $d_{33,f}$. Notably, our findings indicate that a 1.6% O_N can enhance $d_{33,f}$ compared to the oxygen-free state and showing the most significant improvement in the electromechanical coupling coefficient K_{33}^2. Further analysis highlights the key role of Sc and O ions in influencing piezoelectric properties of Sc-doped AlN. Moreover, increasing O_N concentration can raise the dielectric constant $\varepsilon_{r,33}$, enhancing the sensitivity of *w*-$Al_{0.625}Sc_{0.375}N$ to electric stimuli along the *c*-axis. These findings underscore the critical role of precise defect engineering in

optimizing piezoelectric and dielectric properties in Sc-doped AlN, offering valuable insights for applications in sensors, transducers, and other piezoelectric devices.

SUPPLEMENTARY MATERIAL

It includes the detailed geometrical parameters, defect formation energies, piezoelectric tensors, and the average sensitivity of internal parameters for wurtzite $Al_{1-x}Sc_xN$ under various defect types and oxygen concentrations.

ACKNOWLEDGMENTS

SL acknowledges the financial support from Singapore MOE Tier 1 (No. A-8001194-00-00) and Singapore MOE Tier 2 (No. A-8001872-00-00). IMRE authors acknowledge support from A*STAR, under RIE2020 AME Programmatic Fund (Grant No. A20G9b0135), Singapore.

AUTHOR DECLARATIONS

Conflict of interest

The authors have no conflicts to disclose.

Author Contributions

X.W., S.A., L.S and K.Y designed the calculations. X.W. performed the DFT calculations, conducted the theoretical analysis, and drafted the original manuscript. All authors contributed to discussions of the results. L.S. and K.Y. supervised the work, provided input on data analysis, and reviewed and edited the manuscript.

DATA AVAILABILITY

The data that support the findings of this study are available from the corresponding author upon reasonable request.

REFERENCES

[1]R. C. Turner, P. A. Fuierer, R. E. Newnham, and T. R. Shrout, "Materials for High Temperature Acoustic and Vibration Sensors: A Review," *Appl. Acoust.* **41**, 299–324 (1994).

[2]C. Xiong, X. Sun, K. Y. Fong, and H. X. Tang, "Integrated High Frequency Aluminum Nitride Optomechanical Resonators," *Appl. Phys. Lett.* **100**, 171111 (2012).

[3]N. Sinha, G. E. Wabiszewski, R. Mahameed, V. V. Felmetsger, S. M. Tanner, R. W. Carpick, and G. Piazza, "Piezoelectric Aluminum Nitride Nanoelectromechanical Actuators," *Appl. Phys. Lett.* **95**, 053106 (2009).

[4]Y. Saito, H. Takao, T. Tani, T. Nonoyama, K. Takatori, T. Homma, T. Nagaya, and M. Nakamura, "Lead-Free Piezoceramics," *Nature* **432**, 84–87 (2004).

[5]Y. Kusano, G.-L. Luo, D. Horsley, I. Taru Ishii, and A. Teshigahara, "36% Scandium-Doped Aluminum Nitride Piezoelectric Micromachined Ultrasonic Transducers," *IEEE Int. Ultrason. Symp.* **2018**, 1–4.

[6]J. Startt, M. Quazi, P. Sharma, I. Vazquez, A. Poudyal, N. Jackson, and R. Dingreville, "Unlocking AlN Piezoelectric Performance with Earth-Abundant Dopants," *Adv. Electron. Mater.* **9**, 2201187 (2023).

[7]Iwazaki, T. Yokoyama, T. Nishihara, and M. Ueda, "Highly Enhanced Piezoelectric Property of Co-Doped AlN," *Appl. Phys. Express* **8**, 061501 (2015).

[8]M. Akiyama, T. Kamohara, K. Kano, A. Teshigahara, Y. Takeuchi, and N. Kawahara, "Enhancement of Piezoelectric Response in Scandium Aluminum Nitride Alloy Thin Films Prepared by Dual Reactive Cosputtering," *Adv. Mater.* **21**, 593–596 (2009).
[9]M. Akiyama, K. Kano, and A. Teshigahara, "Influence of Growth Temperature and Scandium Concentration on Piezoelectric Response of Scandium Aluminum Nitride Alloy Thin Films," *Appl. Phys. Lett.* **95**, 162107 (2009).
[10]O. Zywitzki, T. Modes, S. Barth, H. Bartzsch, and P. Frach, "Effect of Scandium Content on Structure and Piezoelectric Properties of AlScN Films Deposited by Reactive Pulse Magnetron Sputtering," *Surf. Coat. Technol.* **309**, 417–422 (2017).
[11]M. D. Henry, T. R. Young, E. A. Douglas, and B. A. Griffin, "Reactive Sputter Deposition of Piezoelectric $Sc_{0.12}Al_{0.88}N$ for Contour Mode Resonators," *J. Vac. Sci. Technol. B* **36**, 03E104 (2018).
[12]S. Fichtner, N. Wolff, G. Krishnamurthy, A. Petraru, S. Bohse, F. Lofink, S. Chemnitz, H. Kohlstedt, L. Kienle, and B. Wagner, "Identifying and Overcoming the Interface Originating C-Axis Instability in Highly Sc Enhanced AlN for Piezoelectric Micro-Electromechanical Systems," *J. Appl. Phys.* **122**, 035301 (2017).
[13]C. Höglund, J. Birch, B. Alling, J. Bareño, Z. Czigány, P. O. A. Persson, G. Wingqvist, A. Zukauskaite, and L. Hultman, "Wurtzite Structure $Sc_{1-x}Al_xN$ Solid Solution Films Grown by Reactive Magnetron Sputter Epitaxy: Structural Characterization and First-Principles Calculations," *J. Appl. Phys.* **107**, 123515 (2010).
[14]S. Mertin, B. Heinz, O. Rattunde, G. Christmann, M.-A. Dubois, S. Nicolay, and P. Muralt, "Piezoelectric and Structural Properties of C-Axis Textured Aluminium Scandium Nitride Thin Films up to High Scandium Content," *Surf. Coat. Technol.* **343**, 2–6 (2018).
[15]K. R. Talley, S. L. Millican, J. Mangum, S. Siol, C. B. Musgrave, B. Gorman, A. M. Holder, A. Zakutayev, and G. L. Brennecka, "Implications of Heterostructural Alloying for Enhanced Piezoelectric Performance of (Al, Sc) N," *Phys. Rev. Mater.* **2**, 063802 (2018).
[16]S. K. Ryoo, K. D. Kim, H. W. Park, Y. B. Lee, S. H. Lee, I. S. Lee, S. Byun, D. Shim, J. H. Lee, and H. J. Kim, "Investigation of Optimum Deposition Conditions of Radio Frequency Reactive Magnetron Sputtering of $Al_{0.7}Sc_{0.3}N$ Film with Thickness Down to 20 nm," *Adv. Electron. Mater.* **8**, 2200726 (2022).
[17]M. Akiyama, T. Kamohara, K. Kano, A. Teshigahara, and N. Kawahara, "Influence of Oxygen Concentration in Sputtering Gas on Piezoelectric Response of Aluminum Nitride Thin Films," *Appl. Phys. Lett.* **93**, 021903 (2008).
[18]Z. Ding, X. Cao, Q. Jia, and X. Zhang, "Preparation and Performance of AlSc Alloy Targets," *AIP Conf. Proc.* **2474**, 020029 (2022).
[19]J. Casamento, H. G. Xing, and D. Jena, "Oxygen Incorporation in the Molecular Beam Epitaxy Growth of $Sc_xGa_{1-x}N$ and $Sc_xAl_{1-x}N$," *Phys. Status Solidi B* **257**, 1900612 (2020).
[20]D. Rao, B. Biswas, E. Flores, A. Chatterjee, M. Garbrecht, Y. R. Koh, V. Bhatia, A. I. K. Pillai, P. E. Hopkins, and M. Martin-Gonzalez, "High Mobility and High Thermoelectric Power Factor in Epitaxial ScN Thin Films Deposited with Plasma-Assisted Molecular Beam Epitaxy," *Appl. Phys. Lett.* **116**, 152103 (2020).
[21]P. Gasparotto, M. Fischer, D. Scopece, M. O. Liedke, M. Butterling, A. Wagner, O. Yildirim, M. Trant, D. Passerone, H. J. Hug, and C. A. Pignedoli, "Mapping the Structure of Oxygen-

Doped Wurtzite Aluminum Nitride Coatings from Ab Initio Random Structure Search and Experiments," *ACS Appl. Mater. Interfaces* **13**, 5762–5771 (2021).

[22]Z. Fang, E. Wang, Y. Chen, X. Hou, K.-C. Chou, W. Yang, J. Chen, and M. Shang, "Wurtzite AlN (0001) Surface Oxidation: Hints from Ab Initio Calculations," *ACS Appl. Mater. Interfaces* **10**, 30811–30818 (2018).

[23]J. Kim, J.-Y. Kim, H. Ahn, M. H. Jeong, E. Lee, K. Cho, S.-M. Lee, W. Shim, and J.-H. Pee, "Direct Evidence on Effect of Oxygen Dissolution on Thermal and Electrical Conductivity of AlN Ceramics Using Al Solid-State NMR Analysis," *Mater.* **15**, 8125 (2022).

[24]P. Wang, B. Wang, D. A. Laleyan, A. Pandey, Y. Wu, Y. Sun, X. Liu, Z. Deng, E. Kioupakis, and Z. Mi, "Oxygen Defect Dominated Photoluminescence Emission of $Sc_xAl_{1-x}N$ Grown by Molecular Beam Epitaxy," *Appl. Phys. Lett.* **118**, 032102 (2021).

[25]R. Kumar, S. Nayak, M. Garbrecht, V. Bhatia, A. I. K. Pillai, M. Gupta, S. Shivaprasad, and B. Saha, "Clustering of Oxygen Point Defects in Transition Metal Nitrides," *J. Appl. Phys.* **129**, 055305 (2021).

[26]Q. Yan, A. Janotti, M. Scheffler, and C. G. Van de Walle, "Origins of Optical Absorption and Emission Lines in AlN," *Appl. Phys. Lett.* **105**, 261903 (2014).

[27]J.-M. Mäki, I. Makkonen, F. Tuomisto, A. Karjalainen, S. Suihkonen, J. Räisänen, T. Yu. Chemekova, and Yu. N. Makarov, "Identification of the V_{Al}-on Defect Complex in AlN Single Crystals," *Phys. Rev. B* **84**, 081204 (2011).

[28]S. M. Evans, N. C. Giles, L. E. Halliburton, G. A. Slack, S. B. Schujman, and L. J. Schowalter, "Electron Paramagnetic Resonance of a Donor in Aluminum Nitride Crystals," *Appl. Phys. Lett.* **88**, 062112 (2006).

[29]N. T. Son, A. Gali, Á. Szabó, M. Bickermann, T. Ohshima, J. Isoya, and E. Janzén, "Defects at Nitrogen Site in Electron-Irradiated AlN," *Appl. Phys. Lett.* **98**, 242116 (2011).

[30]C.-W. Lee, N. U. Din, G. L. Brennecka, and P. Gorai, "Defects and oxygen impurities in ferroelectric wurtzite $Al_{1-x}Sc_xN$ alloys," *Appl. Phys. Lett.* **125**, 022901 (2024).

[31]Z. Liu, X. Wang, X. Ma, Y. Yang, and D. Wu, "Doping effects on the ferroelectric properties of wurtzite nitrides," *Appl. Phys. Lett.* **122**, 122901 (2023).

[32]S. Acharya, X. Wang, Q. Xu, M. Zhang, J. Chai, P. Luo, P. C. Lim, P. Yang, L. Shen, C. Sun, and K. Yao, "Role of Oxygen on Structure and Piezoelectric Properties of $Al_{0.65}Sc_{0.35}N$ Thin Films," *Phys. Rev. Appl.* **22**, 044071 (2024).

[33]G. Kresse and J. Furthmüller, "Efficiency of Ab-Initio Total Energy Calculations for Metals and Semiconductors Using a Plane-Wave Basis Set," *Comput. Mater. Sci.* **6**, 15–50 (1996).

[34]G. Kresse and J. Furthmüller, "Efficient Iterative Schemes for Ab Initio Total-Energy Calculations Using a Plane-Wave Basis Set," *Phys. Rev. B* **54**, 11169 (1996).

[35]P. E. Blöchl, "Projector Augmented-Wave Method," *Phys. Rev. B* **50**, 17953 (1994).

[36]J. P. Perdew, K. Burke, and M. Ernzerhof, "Generalized Gradient Approximation Made Simple," *Phys. Rev. Lett.* **77**, 3865 (1996).

[37]J. P. Perdew, A. Ruzsinszky, G. I. Csonka, O. A. Vydrov, G. E. Scuseria, L. A. Constantin, X. Zhou, and K. Burke, "Restoring the Density-Gradient Expansion for Exchange in Solids and Surfaces," *Phys. Rev. Lett.* **100**, 136406 (2008).

[38]S. Grimme, S. Ehrlich, and L. Goerigk, "Effect of the Damping Function in Dispersion Corrected Density Functional Theory," *J. Comput. Chem.* **32**, 1456–1465 (2011).

[39]H. J. Monkhorst and J. D. Pack, "Special Points for Brillouin-Zone Integrations," *Phys. Rev. B* **13**, 5188 (1976).
[40]S. B. Zhang and J. E. Northrup, "Chemical potential dependence of defect formation energies in GaAs: Application to Ga self-diffusion," *Phys. Rev. Lett.* **67**, 2339 (1991).
[41]G. Herzberg, *Molecular Spectra and Molecular Structure: Volume I*, Read Books Ltd., 2013.
[42]X. Zhang, J. Kang, and S.-H. Wei, "Defect modeling and control in structurally and compositionally complex materials," *Nat. Comput. Sci.* 3, 210 (2023).
[43]S. Baroni, S. De Gironcoli, A. Dal Corso, and P. Giannozzi, "Phonons and Related Crystal Properties from Density-Functional Perturbation Theory," *Rev. Mod. Phys.* **73**, 515 (2001).
[44]M. Noor-A-Alam, O. Z. Olszewski, H. Campanella, and M. Nolan, "Large Piezoelectric Response and Ferroelectricity in Li and V/Nb/Ta Co-Doped Wurtzite AlN," *ACS Appl. Mater. Interfaces* **13**, 944–954 (2021).
[45]M. A. Caro, S. Zhang, M. Ylilammi, T. Riekkinen, M. A. Moram, O. Lopez-Acevedo, J. Molarius, and T. Laurila, "Piezoelectric coefficients and spontaneous polarization of ScAlN," *J. Phys. Condens. Matter*. **27**, 245901 (2015).
[46]Tagami, J. Koga, Y. Nohara, and M. Usami, "Origin of Enhanced Piezoelectric Constants of MgNbAlN Studied by First-Principles Calculations," *Jpn. J. Appl. Phys.* **56**, 058004 (2017).
[47]C. Tholander, F. Tasnádi, I. A. Abrikosov, L. Hultman, J. Birch, and B. Alling, "Large Piezoelectric Response of Quaternary Wurtzite Nitride Alloys and Its Physical Origin from First Principles," *Phys. Rev. B* **92**, 174119 (2015).
[48]M. Noor-A-Alam, O. Z. Olszewski, and M. Nolan, "Ferroelectricity and Large Piezoelectric Response of AlN/ScN Superlattice," *ACS Appl. Mater. Interfaces* **11**, 20482–20490 (2019).
[49]F. Bernardini, V. Fiorentini, and D. Vanderbilt, "Spontaneous Polarization and Piezoelectric Constants of III–V Nitrides," *Phys. Rev. B* **56**, R10024 (1997).
[50]M. Akiyama, K. Umeda, A. Honda, and T. Nagase, "Influence of Scandium Concentration on Power Generation Figure of Merit of Scandium Aluminum Nitride Thin Films," *Appl. Phys. Lett.* **102**, 021915 (2013).
[51]Q. Wang, Y. Lu, S. Mishin, Y. Oshmyansky, and D. A. Horsley, "Design, Fabrication, and Characterization of Scandium Aluminum Nitride-Based Piezoelectric Micromachined Ultrasonic Transducers," *J. Micromech. Syst.* **26**, 1132–1139 (2017).
[52]V. T. Rathod, "A Review of Acoustic Impedance Matching Techniques for Piezoelectric Sensors and Transducers," *Sensors* **20**, 4051 (2020).
[53]G. Esteves, T. R. Young, Z. Tang, S. Yen, T. M. Bauer, M. D. Henry, and R. H. Olsson, "$Al_{0.68}Sc_{0.32}N$ Lamb Wave Resonators with Electromechanical Coupling Coefficients near 10.28%," *Appl. Phys. Lett.* **118**, 171902 (2021).
[54]S. Manna, G. L. Brennecka, V. Stevanović, and C. V. Ciobanu, "Tuning the Piezoelectric and Mechanical Properties of the AlN System via Alloying with YN and BN," *J. Appl. Phys.* **122**, 105101 (2017).
[55]G. Wingqvist, F. Tasnádi, A. Zukauskaite, J. Birch, H. Arwin, and L. Hultman, "Increased Electromechanical Coupling in *w*–$Sc_xAl_{1-x}N$," *Appl. Phys. Lett.* **97**, 112902 (2010).